



Article

Cross-Domain Submesoscale Eddy Detection Neural Network for HF Radar

Fangyuan Liu ^{1,*} , Hao Zhou ^{1,*} , Weimin Huang ² , Yingwei Tian ^{1,3} and Biyang Wen ¹

¹ The School of Electronic Information, Wuhan University, Wuhan 430072, China; liufy@whu.edu.cn (F.L.); tianyw@whu.edu.cn (Y.T.); bywen@whu.edu.cn (B.W.)

² The Faculty of Engineering and Applied Science, Memorial University of Newfoundland, St. John's, NL A1B 3X5, Canada; weimin@mun.ca

³ Key Laboratory of Marine Environmental Survey Technology and Application, Ministry of Natural Resources, Guangzhou 528428, China

* Correspondence: zhou.h@whu.edu.cn

Abstract: With the rapid development of deep learning, the neural network becomes an efficient approach for eddy detection. However, previous work employs a traditional neural network with a focus on improving the detecting accuracy only using limited data under a single scenario. Meanwhile, the experience of detecting eddies from one experiment is not directly inherited from the detection model for other experiments. Therefore, a cross-domain submesoscale eddy detection neural network (CDEDNet) based on the high-frequency radar (HFR) data of the Nansan and Xuwen region is proposed in this paper. Firstly, a fundamental deep eddy detection architecture CDEDNet-0 is constructed with a fully convolutional network (FCN). Secondly, for solving the problem of insufficient labeled eddy data, an instance-based domain adaption method is adopted in CDEDNet-1 to increase training samples. Thirdly, for tackling the problem of unable to inherit previous detection experience, parameter-based transfer learning is incorporated in CDEDNet-2 for multi-scene eddy detection. The experiment results demonstrate CDEDNet-1 and CDEDNet-2 perform better than CDEDNet-0 in terms of accuracy. Meanwhile, eddy characteristics including eddy type, radius, occurring time, merger, and dynamic trajectory are analyzed for the Nansan and Xuwen regions.

Keywords: eddy detection; deep learning; cross-domain learning; high-frequency radar



Citation: Liu, F.; Zhou, H.; Huang, W.; Tian, Y.; Wen, B. Cross-Domain Submesoscale Eddy Detection Neural Network for HF Radar. *Remote Sens.* **2021**, *13*, 2441. <https://doi.org/10.3390/rs13132441>

Academic Editor: Fabio Del Frate

Received: 23 April 2021

Accepted: 16 June 2021

Published: 22 June 2021

Publisher's Note: MDPI stays neutral with regard to jurisdictional claims in published maps and institutional affiliations.



Copyright: © 2021 by the authors. Licensee MDPI, Basel, Switzerland. This article is an open access article distributed under the terms and conditions of the Creative Commons Attribution (CC BY) license (<https://creativecommons.org/licenses/by/4.0/>).

1. Introduction

An oceanic eddy is a circular current of sea water [1–3]. The largest scale oceanic eddies are caused by the instability of horizontally sheared motion typically seen in boundary current, while relatively smaller (on a horizontal scale of tens of kilometers) eddies such as baroclinic eddies are generated by the sudden severe change of sea water's transverse density gradient associated with baroclinic instability [4,5]. According to the rotation directions, oceanic eddies can be divided into cyclonic eddies and anticyclonic eddies. They can also be divided into different categories according to their sizes. In oceanography, mesoscale eddies normally refer to eddies with a horizontal scale of tens to hundreds of kilometers and they can survive for several days to 1 year [6–8]. Submesoscale eddies are those with a smaller horizontal scale on the order of 1 km and they only survive for a period of a few hours to several days [9–11]. Although mesoscale eddies have a larger diameter and a lifetime of days and weeks, there are also smaller short-living eddies (e.g., in frontal filaments, behind the coastal and topographic features). In the ocean, mesoscale and submesoscale eddies transport particles, debris, and organisms and transfer heat, mass, and oxygen in both horizontal and vertical directions, which play a critical role in the marine ecosystem and environment [12–15]. Besides, eddies may appear on shipping routes and in offshore regions and affect human marine activity. Therefore, the detection and tracking of mesoscale and submesoscale eddies are significant.

The primary objective of eddy detection is to determine the eddy center, radius, and boundary [16]. Three typical equipments used to collect eddy data are in-situ sensor [17], satellite [18] and high-frequency radar (HFR) [16,19]. An in-situ sensor is good for eddies in a small-scale region, but it cannot provide complete eddy information when an eddy randomly occurs in a large-scale region. In other words, only when the eddy location can be predicted in advance, the in-situ sensor is effective. Thus, an in-situ sensor is seldom utilized in a region with unpredictable eddies. Satellite sensor is useful for large-area, long-period, and multi-type eddy observation since it has a large field of view. However, sea surface height (SSH) and sea level anomaly (SLA) results from satellite data are characterized by a low spatial resolution (larger than $0.25^\circ \times 0.25^\circ$) and a long revisit period (far more than 1 h). HFR can accurately measure offshore eddy parameters due to its relatively higher spatial resolution ($0.03^\circ \times 0.03^\circ$) and near real-time observation capability (every 20 min). So far, HFR is the most efficient equipment for submesoscale eddy monitoring.

The detection of oceanic eddy depends on the geometry characteristic of the eddy. The spiral structure of an eddy in the three-dimensional (3D) space can be well studied by a projection onto the two-dimensional (2D) plane, where the sea surface vector currents show an obvious rotating structure. For the continuity of the fluid, there should be a vertical current component to compensate for the non-zero 2D divergence, so a more detailed eddy structure can be retrieved by deploying more sensors in the 3D space. Existing eddy detection methods fall in four categories: expert-based visual method [20], physics-based statistics method [21], geometry-based statistics method [22], and deep learning-based method [23]. The expert-based visual method depends on the expert's experience and visual judgment to distinguish eddies. It is the most reasonable method but requires significant labor effort. Such detection results are usually used as ground truth. The physics-based statistic method detects eddies according to whether the values of certain physical quantities are higher than a threshold, such as pressure, the current's speed, vorticity, and helicity. The physics-based method searches for the outermost closed contour of the streamlines as the eddy boundary and the zero-speed position within the eddy boundary as the eddy center. The classical physics-based method is the Okubo-Weiss method [24], which employs three direct indices, including shearing deformation rate, straining deformation rate, and vorticity, for determining the existence of an eddy. The geometry-based statistic method detects eddies by checking whether the eddy's pattern satisfies geometric criteria according to the eddy's shallow features extracted. The representative geometry-based methods include vector-geometry (VG) [25] and winding-angle (WA) [26] methods. The VG method utilizes four different constraint conditions to locate the eddy center, and then it treats the center's outermost closed streamline contour as the eddy boundary. The WA method firstly implements clustering operation to determine the streamline centers and then regards the streamline centers of the same cluster as the eddy center, finally, it fits streamlines of the same cluster as the eddy boundary. Deep learning-based methods include object detection-like pipelines and pixel segmentation-like pipelines. Deep eddy detection means using deep learning-based methods to implement the eddy detection task. In the first pipeline, eddy detection is regarded as an object detection task. The object detection network firstly identifies the candidate region possibly with the eddy, then reduces the area of the candidate region, and then generates a bounding box without an overlapped area, finally, it uses the VG method for localizing the eddy center and computing the eddy boundary in the bounding box. The performance of the first pipeline depends significantly on the VG's detection capacity. Deep learning is only applied for the feature extraction and bounding box. Therefore, the researchers attempt to develop an end-to-end network to make full use of deep learning for eddy detection. In the second pipeline, eddy detection is regarded as a pixel segmentation task. The pixel segmentation network takes the original current field as input and directly outputs the identified pixels associated with cyclonic eddies, anticyclonic eddies, and background. The second pipeline is convenient for the oceanologist since they need little deep learning knowledge but

can rapidly identify the eddies. Meanwhile, the black-box-like structure of the second pipeline provides the users with little flexibility to alter the module, which may lead to a performance lower than the first pipeline. In this work, we incorporate the transfer learning technology into the end-to-end pixel segmentation pipeline for improving its performance in eddy detection.

However, two challenges remain in actual eddy detection using HFR data. The first is that effective labeled data are always insufficient and much less than collected data since visually labeling all the data is impossible and labeling takes much labor and time. Furthermore, labeling the collected data only by an expert's visual judgment is quite inefficient. Fortunately, although the amount of labeled eddy data is small in each experiment, the number of HFR's observation experiments is increasing with the spreading of HFR. The labeled data from other experiments can be shared for public access to augment the training datasets. In this study, we attempt to use instance-based domain adaptation to increase training samples using previous similar observation data.

The second challenge is how to inherit experience from previous detection [27]. As for classical eddy detection methods, past detection results including fuzzy perception, threshold, and parameters from a previous analysis may give limited assistance to the construction of a detection model in the present application. When the observation area is the same, the model trained previously may be adopted. When the area is different, the direct application of previous models may cause problems. Because the network trained for one region (e.g., Mediterranean) may recognize some exclusive characteristics of the eddy in that area but if they do not exist in the other region (e.g., Malacca Strait), redesigning or retraining of the network is necessary. Moreover, previous deep models are mainly developed for the regions with enough data (e.g., Mediterranean and Australian's Coral Sea regions), while the regions with insufficient data (e.g., Cape of Good Hope and Malacca Strait) attract only a little attention. The transfer learning technology can be used to identify and discard specific regional characteristics and retain common eddy characteristics, then the data imbalance problem can be solved even if the data are insufficient. Here, we attempt to use parameter-based transfer learning by sharing a general feature layer for eddy detection in multiple regions.

In this paper, a cross-domain eddy detection neural network, CDEDNet, is proposed for HFR applications. Here, cross-domain means analyzing the eddy in one region using the network trained with the eddy data collected from another region. Firstly, a fully convolutional network skeleton-based eddy detection network CDEDNet-0, which is developed using the HFR data from the South China Sea is presented. Secondly, for dealing with the problem of insufficient labeled data, we present an instance-based domain adaptation method for increasing training samples in CDEDNet-1. Thirdly, for dealing with the problem of inheriting previous detection experience, CDEDNet-2 which incorporates parameter-based transfer learning, is designed for multi-scene eddy detection. The remaining content of the paper is organized as follows. Section 2 introduces the related work of deep eddy detection and transfer learning. In Section 3, the HFR systems and data are illustrated. Section 4 describes the structure and loss metric of three CDEDNets. Section 5 demonstrates the performance evaluation and observation analysis. Section 6 contains the conclusion and future plan.

2. Related Work

With the rapid development of deep learning, deep learning-based eddy detection attracts significant interest. In [28], the Ocean Eddy Identification Neural Network (OEDNet) was presented for locating mesoscale eddies automatically. OEDNet is constructed on the skeleton of RetinaNet. It searches for mesoscale eddies with a small number of samples and multiple sea level anomaly (SLA) data. In [29], an eddy identification and tracking framework was proposed based on SLA data from Australia. The framework combines a convolutional neural network for feature learning and the VG method for identifying the eddy's location and shape. In [30], an artificial intelligence idea was adopted for eddy

detection using PSPNet and the VG method. However, its performance is almost the same as the VG method. Because object detection-like pipeline depends on the VG algorithm to determine the eddy's center and boundary, its performance is limited by the VG algorithm to a large extent.

Some researchers attempt to use an end-to-end neural network to transform the current field to the final eddy detection. In [31], a neural network-based ocean eddy current pixel classification framework (EddyNet) was presented for detecting eddies. EddyNet consists of a U-shape neural network (U-Net) structure with a pixel-wise classification layer and uses Copernicus Marine Environment Monitoring Service (CMEMS) SSH maps for exploring eddies. Its classification results are worse than that of statistic-based methods due to limited training data and the closed-contour identification method. In [32], a CNN-based classifier for detecting Mediterranean Sea eddy using SST images was designed. It uses two labeled datasets for model training. The results demonstrate that the model based on a manually annotated dataset performs better than using an automatically annotated dataset. In [33], a dubbed DeepEddy which involves two principal component analysis (PCA) convolution layers for exploiting eddy features and a non-linear transformation for transforming features was developed. DeepEddy utilizes multi-scale features fusion technology in synthetic aperture radar (SAR) images. Its performance is comparable with the statistic-based method, but its computation load is higher. These end-to-end neural networks are based on pixel segmentation neural networks. Although they perform well in predicting the eddy's position, their performance significantly relies on the quality of labeled data and the choice of neural network. Therefore, our work follows the end-to-end roadmap to construct the fundamental CDEDNet and improves the model's performance through instance-based domain adaption and parameter-based transfer learning.

3. Data Description

Our experiment of eddy detection is based on the sea surface current data collected by the Ocean State Monitoring and Analyzing Radar, model S (OSMAR-S), which is a compact HFR system designed by Wuhan University. At 13 MHz, one radar provides a radial current map up to 100 km offshore with a range resolution of 2.5 km every 6.5 min, and two radars at different locations provide a vector current map on a longitude/latitude grid with a uniform spacing of 0.05 degrees in both dimensions every 20 min. OSMAR-S uses monopole as the transmitting antenna and monopole/cross-loop antenna to receive echoes. The sweep bandwidth is 60 kHz and the average transmit power is 100 W. For more details about OSMAR-S, the reader can refer to [34,35].

Some control-quality assurance (QC-QA) measures have been implemented in the current mapping software as well as the hardware of OSMAR-S. An automatic frequency selection module based on noise spectrum monitoring [36] provides the optimum work frequency, i.e., with the lowest noise floor, to ensure the best signal quality for each processing cycle. Before surface current estimation, radio frequency interference (RFI) and instantaneous interference are detected and removed if they are detected [37]. In the radial current map generation, a quality factor is calculated for each radial current based on its corresponding signal-to-noise ratio (SNR) and spatial spectrum, and it is used to decide whether this radial result is valid and its weight in subsequent processing of merging and interpolation (if this radial passes the test). The quality factors for radials are also used for vector current calculation. Median filters in both temporal and space domains are used to remove the weird values in both radials and vectors. Here, the QC test generally follows [38]. With such QC-QA measures, high-quality sea current data can be obtained although a small number of outliers still pass the test especially those on the boundary or baseline. Typical root-mean-square errors (RMSEs) in OSMAR-S are 10–15 cm/s for radials, and 10–16 cm/s in magnitude, and 10–20 degrees in direction for vector current.

This study involves two sets of OSMAR-S data at different times and locations. In the first dataset, two OSMAR-S radars were deployed at Shanliao and Xian in the Fujian province of China. The observation region covers the southwest of the Taiwan Strait and

the experiment period lasts for 80 days, from 11 January 2013 to 31 March 2013. The sample period of OSMAR-S is 20 min, and the total number of generated current fields is 5760. In the second dataset, the same OSMAR-S radars were deployed at Nansan and Xuwen in the Guangdong province of China. The observation region covers the overlapped area between the north of Qiongzhou straits and east of the Leizhou Peninsula in the South China Sea. The 88-day observation period is from 25 July 2017 to 21 October 2017. With the same sample rate, a total number of 5904 current field maps were generated. In both radar current datasets, the effective data rate at each grid point was greater than 0.85. In practical observations, data were missing or of very low quality (e.g., significantly contaminated by noise) for some periods. The effective data rate was calculated as the ratio of the period with useful data over the whole observation period. The high data rate of radar measurement ensured adequate samples for further eddy detection algorithms. Figure 1 depicts the two observation regions. Figure 2 shows the geometric dilution of precision (GDOP) for the current maps in Figure 1. As can be seen, the GDOP had large values near the baseline and greater values near the boundaries and thus, the current measurements in these regions were less reliable than those in the central region. However, the effect of corresponding outliers on our eddy detection results was negligible since eddies were not in these questionable regions in this study (as can be seen in the following figures showing eddies).

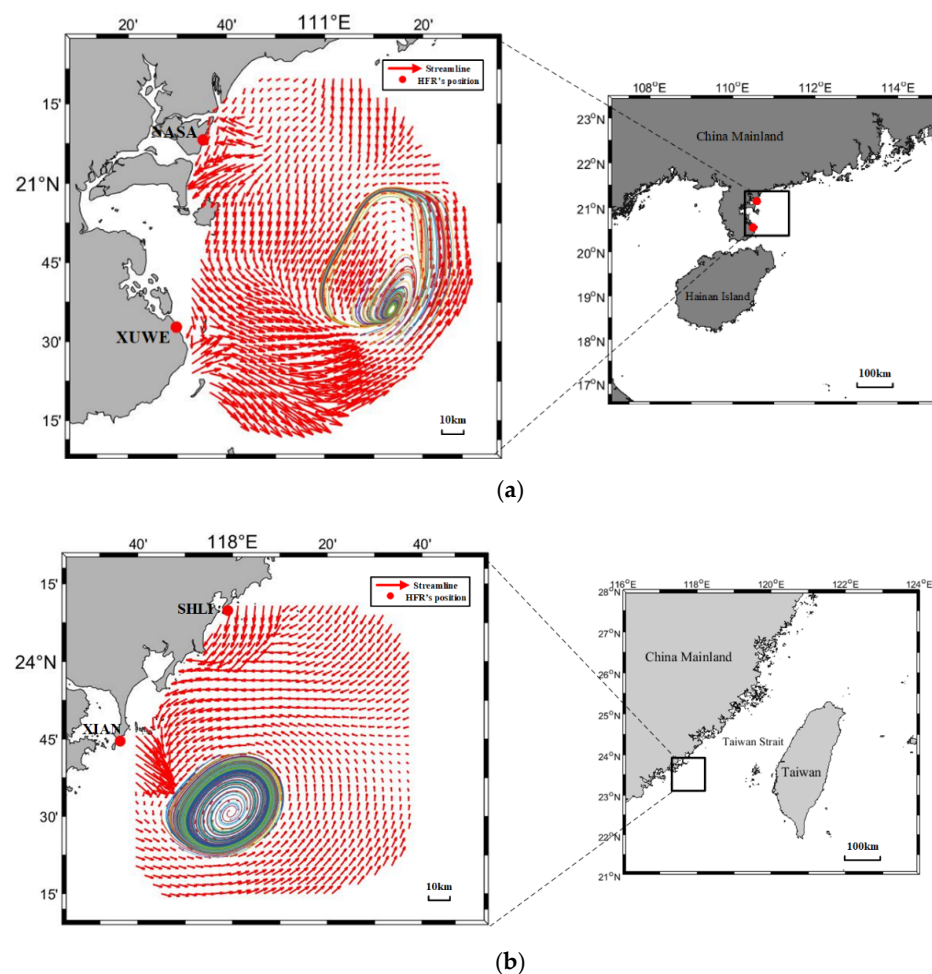


Figure 1. Two different observation regions of Ocean State Monitoring and Analyzing Radar, model S (OSMAR-S). (a) Taiwan Strait and (b) South China Sea. The left columns are the observation results. The red arrows represent current and color lines show the eddy's streamlines. The red spots denote the high-frequency radar (HFR) sites. The right columns are the wide view of the observation region.

For cross-domain eddy detection, one geographical dataset was selected as source data and another as target data. Considering that deep eddy detection had been implemented for the Taiwan Strait dataset [39] and the small number of eddy observations associated with the South China Sea, the Taiwan Strait dataset was chosen as the source data, and the South China Sea dataset was regarded as the target data. The source data consisted of 600 current field images (300 cyclonic eddies and 300 anticyclonic eddies) and their corresponding labeled images. The 600 images were carefully sorted according to common obvious eddy results identified by DEDNet's and the python-eddy-tracker software (PET-14). After that, the expert adjusted the 600 images' results by visual correcting and transformed them to the source data. The target data consisted of 5904 current field images. Wherein, 2000 of them were annotated by PET-14 (PET-14 is an auxiliary eddy detection software and cannot represent ground-truth results). After being annotated by PET-14, each labeled current field image consisted of three categories of pixels: (1) the white pixel represented the background or no eddy data; (2) the red pixel represented cyclonic eddy, and; (3) the green pixel represented anticyclonic eddy. Figure 3 depicts an example of the eddy detection training couple. The left panel of Figure 3 is the original current field map, and the right panel is the segmentation result obtained by PET-14.

Next, CDEDNet was used in the target data to determine the eddy position and determine the eddy type in the remaining 3904 images.

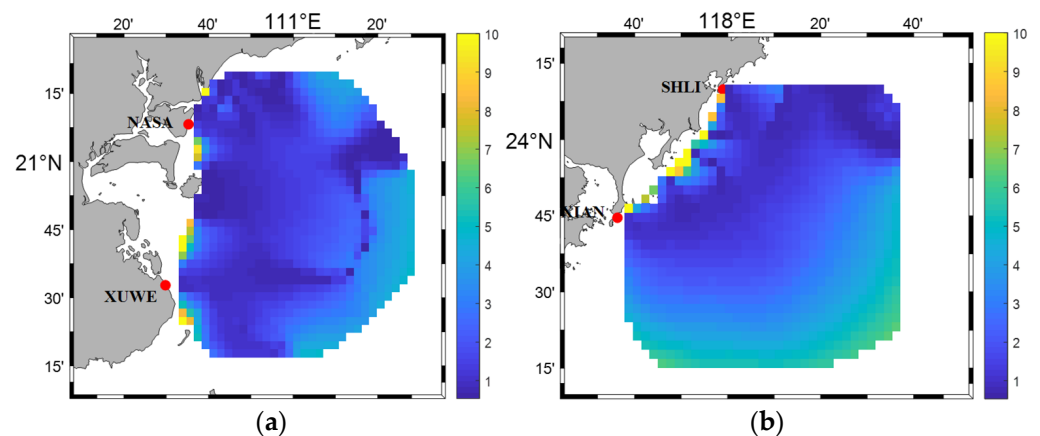


Figure 2. Geometric dilution of precision (GDOP) for the current maps shown in Figure 1a,b. GDOP values greater than 10 are set to 10 for better contrast.

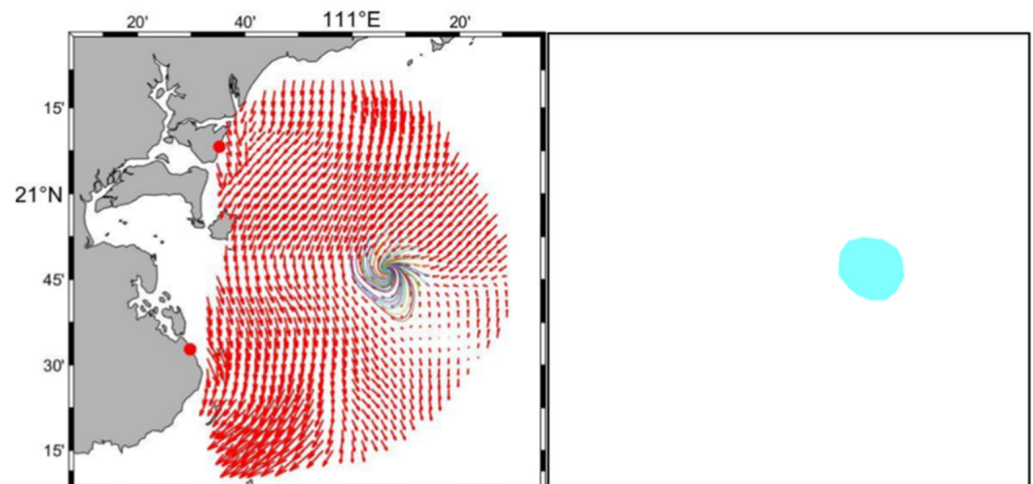


Figure 3. Example of the pixel segmentation training couple.

4. CDEDNets

4.1. Fundamental Architecture

In the first architecture CDEDNet-0 (see Figure 4), our purpose was to implement eddy detection on the radar data from the Nansan and Xuwen (NSXW) sites (i.e., the South China Sea dataset). The dataset contained 5904 current fields, wherein 2000 were annotated by PET-14. The aim was to determine the eddy parameters of the remaining 3904 current field maps. Here, the eddy situation referred to no eddy, one eddy, or multiple eddies in a current field map. In the final detection results, each pixel was classified and the eddy type determined.

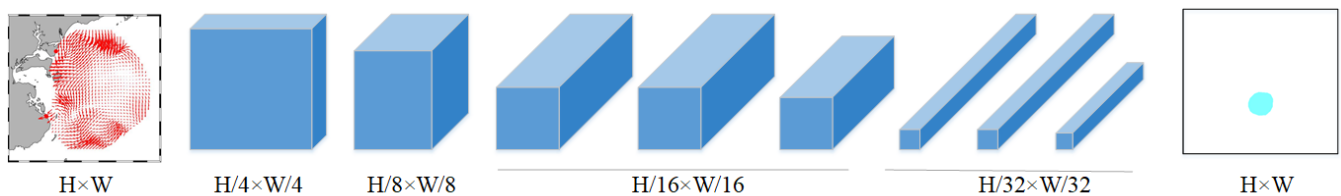


Figure 4. Cross-domain submesoscale eddy detection neural network (CDEDNet-0): Fundamental Architecture. The 8 blue cuboids correspond to 8 convolution layers. For each cuboid, the three dimensions are the height and width of its input image and the number of its output feature map. The leftmost map is the original current field. The rightmost map is the predicted eddy mask by CDEDNet-0.

CDEDNet-0 is an FCN-based neural network, i.e., it is constructed with a fully convolutional network and contains 8 convolution layers and upsampling operator. Figure 4 depicts its fundamental architecture for detecting eddies from the South China Sea datasets. The size of the input current map was mainly determined by the radar coverage. OSMAR-S can cover a region up to 100 km. The vector current maps were generated on latitude/longitude grids with a resolution of 0.05 degrees in both dimensions. Here we used linear interpolation to produce the current maps each consisting of 832×576 grids (pixels). The first convolution layer extracted the flow chart's feature from the current map and implemented the pooling operator, which reduced the size to 208×144 pixels. The second convolution layer also extracted the flow chart's feature and implemented the pooling operator, which reduced the size to 104×72 pixels. The subsequent three convolution layers further reduced the size to 52×36 pixels, and the last three convolution layers reduced the size to 26×18 pixels. The image with a size of 26×18 pixels was referred to as the heatmap. Then, the upsampling operator transformed the heatmap to a feature map, whose size was the same as the original current field. The final feature map showed background, cyclone, and anticyclone at the pixel level.

Different from a regular convolution neural network (CNN), FCN replaces the last three full connection layers with convolution layers, which enables classification at the pixel level. Meanwhile, FCN can take images of arbitrary size as input and maintain the space information of the original current field. Besides that, CDEDNet-0 adopts cross-entropy loss as a loss function because combining the softmax function with cross-entropy loss is common in the classical segmentation network. Other options may have a high computation load. CDEDNet-0 adopts stochastic gradient descent (SGD) as the optimizing strategy and K-fold cross-validation ($K = 10$) for training because SGD has a faster computation speed than Batch Gradient Descent (BGD) and K-fold cross-validation can effectively prevent the training process from overfitting.

4.2. Architecture with Instance-Based Domain Adaption

Since the incorporation of the new dataset is beneficial to improve the original neural network's performance, the second architecture CDEDNet-1 was designed for eddy detection using the same dataset with the aid of another similar dataset. Different from CDEDNet-0, the instance-based domain adaption technology was applied to enlarge the training dataset and enhance the learning. Besides the former South China Sea datasets, the

radar data from the Xiaan and Shanliao (XASL) sites (i.e., the Taiwan strait dataset) were also used. Except the observation systems being the same (OSMAR-S), the observation region and observation period were different between these two datasets. Meanwhile, the XASL dataset included only 600 manually annotated current field images (300 cyclonic eddies and 300 anticyclone eddies). Therefore, we decided to increase the training samples by transferring XASL's accurate annotated images. The 600 current field images of the XASL dataset were regarded as source data and 2000 current field images of the NSXW dataset were used as target data.

Figure 5 depicts the CDEDNet-1 architecture which incorporates instance-based domain adaption for detecting eddies. The difference in observation region and period lead to the difference in marginal and conditional distribution between the NSXW and XASL datasets, therefore, direct supplement from XASL to NSXW dataset was unfeasible. It was necessary to use domain adaption technology for mapping them into a common space. In domain adaption, the source and target data are first mapped to a candidate feature space by a fixed weight of marginal and conditional distribution. The mapping method is based on PCA. PCA is an algorithm to orthogonally transform the columns of a dataset into a new set of features called principal components and is thus able to analyze data features in a smaller dimension via data dimension reduction. Next, in the new feature space, maximum mean discrepancy (MMD) was computed for evaluating the difference degree between the source and target data. If the MMD index could not satisfy the adaption requirements, the mapping was modified according to the traceback of distribution difference till the requirement was satisfied. The feature space at the termination of mapping served as the shared space for both data. Then, the mapped source and target data were used as the new training samples for the FCN-based eddy detection network. Finally, the well-trained network was used to determine the eddy situation for the remaining current fields of the NSXW dataset.

There were two primary differences between CDEDNet-1 and CDEDNet-0. The first was the quantity and quality of training samples. CDEDNet-0 only used 2000 automatically annotated current fields as training data, but CDEDNet-1 added 600 accurately and manually annotated samples to the training dataset. The second difference was the computation load. It was obvious that CDEDNet-1 had a higher computation load due to domain adaption. The differences made the two architectures suitable for different situations. CDEDNet-1 was more suitable for the application where collected data were insufficient but extra high-quality similar data from elsewhere were available.

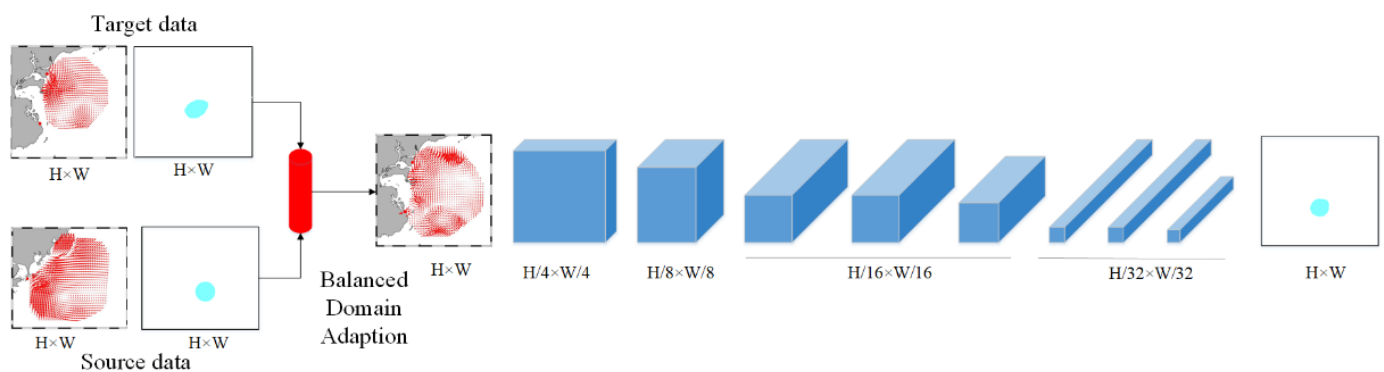


Figure 5. CDEDNet-1: Architecture with Instance-based Domain Adaption. The 8 blue cuboids correspond to 8 convolution layers. For each cuboid, the three dimensions are the height and width of its input image and the number of its output feature maps. The leftmost maps are the original current fields. The rightmost map is the predicted eddy mask by CDEDNet-1.

4.3. Architecture with Parameter-Based Transfer Learning

In the third architecture CDEDNet-2, other neural network layers trained with similar data were incorporated. In fact, [39] presents an FCN-based neural network FCN-1 for eddy detection from the XASL dataset. Both CDEDNet-2 and FCN-1 are for detecting am

eddy from HFR's current field, but for data collected from different observation regions and periods. Therefore, we decided to transfer the structure and parameters trained in FCN-1 to CDEDNet-2.

Here, CDEDNet-2 directly adopted the first seven convolution layers of FCN-1 and only changed the weight of the last layer randomly. Figure 6 depicts the architecture of CDEDNet-2 which incorporates parameter-based transfer learning. Because FCN-1 already had the capacity for extracting the general features of both cyclonic and anticyclonic eddies, and little difference existed between the XASL and NSXW datasets, by using the same first seven convolution layers, the general eddy detection capacity of FCN-1 was inherited to CDEDNet-2. Only the last convolution layer of CDEDNet-2 needed to be retrained to be applicable for specific eddy features in the NSXW dataset. After CDEDNet-2 was trained with 2000 images from the NSXW dataset, it could be used to identify the eddy in the remaining current field dataset.

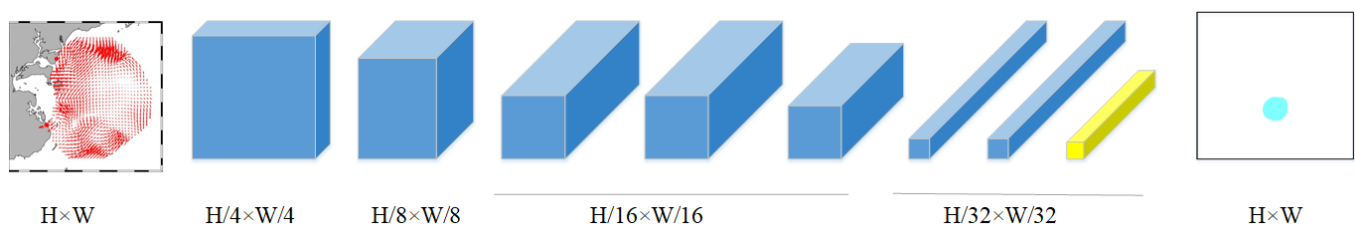


Figure 6. CDEDNet-2: Architecture with Parameter-based Transfer Learning. The 8 blue cuboids correspond to 8 convolution layers. The leftmost map is the original current field. The rightmost map is the predicted eddy mask by CDEDNet-2.

The main difference between CDEDNet-2 and CDEDNet-0 lied in two aspects. The first was the number of parameters to be tuned. CDEDNet-0 needed to tune all the parameters on 8 convolution layers. CDEDNet-2 only needed to train the parameters of the last layer. The second was the training time. Since fewer parameters needed to be trained, CDEDNet-2 could be trained much faster.

5. Test Results and Discussion

All the three architectures introduced earlier were implemented on the Tensorflow backend of the Pytorch framework. The hardware platform included an Intel I5-6600K CPU at 3.5GHz and an NVidia GTX 1060 GPU card with a 6 GB memory. The training dataset of CDEDNet-0 only contained 2000 automatically annotated current field maps. The training dataset of CDEDNet-1 consisted of 2000 automatically annotated current fields and 600 transferred manually annotated current maps. The CDEDNet-2 only used 2000 automatically annotated current maps and the pretrained FCN-based eddy detection neural network based on the XASL dataset. The ground truth results were obtained based on the results from PET-14, the VG and WA algorithms, as well as expert visual observation. This method produced the most accurate ground truth results with the least labor cost.

5.1. Fundamental Architecture

The three architectures were sequentially implemented for eddy detection from the NSXW dataset. Figure 7 depicts the eddy detection results of three architectures. Figure 7a is the original current field, which mainly shows the current, coastline, and HFR site. Figure 7b shows the ground-truth result obtained using a combinational method based on PET-14, the VG algorithm, the WA algorithm, and expert visual observation. Figure 7c–e represents the detection results obtained by CDEDNet-0, CDEDNet-1, and CDEDNet-2, respectively. Predicted masks were obtained as the processing output in Figure 7c–e, which represent the eddy positions in the original current fields.

The ground-truth results clearly depicted a distinct eddy boundary and the wrapper gradation of the streamline. The eddy boundaries detected by CDEDNets were more or less influenced by the surrounding streamline features. Wherein, the eddy boundary

obtained from CDEDNet-0 was difficult to be recognized, e.g., the result from the third row of (c) shows obvious error. It could be concluded that CDEDNet-1 and CDEDNet-2 performed better than CDEDNet-0, but it was difficult to distinguish the difference between the performances of CDEDNet-1 and CDEDNet-2.

CDEDNet-1 and CDEDNet-2 had similar performance in identifying the boundary. The eddy in the image of the first row showed relatively complex streamlines. It was not a perfect elliptic eddy but had both sparse and dense streamlines. However, CDEDNet-1 and CDEDNet-2 performed well for this current field. The boundaries identified by them were approximately the outermost closed curve. As for eddy location, all three CDEDNets obtained results that agreed well with the ground-truth data.

A quantitative comparison of the three CDEDNets was also conducted. Table 1 lists the accuracy comparison from 30 experiments. In Table 1, the accuracy for each eddy type is defined as the ratio of correctly detected positive samples over all true positive samples of that type. Additionally, IoU means Intersection over Union. CDEDNet-1, CDEDNet-2, and CDEDNet-0 ranked, respectively, first, second and third in terms of accuracy. Wherein, the results of CDEDNet-1 and CDEDNet-2 were close to each other, with a difference of only 0.009. The detection accuracies of cyclonic eddies and no eddies were higher than that of anticyclonic eddies. This was partially due to the imbalance of samples in the categories. The number of anticyclonic eddies was less than that of cyclonic eddies and there were no eddies in the training data.

In conclusion, CDEDNet-1 and CDEDNet-2 were better than CDEDNet-0. CDEDNet-1 benefited from the additional transferred similar data for training. Enlarged training data size improved the model performance. With more and more HFRs being installed, CDEDNet-1 has the potential for wide application. CDEDNet-2 benefited from the frozen general eddy feature layers trained from other detection experiments. The special NSXW's eddy feature could be directly identified from the 2000 training images. As a result, CDEDNet-2 improved the accuracy by 0.062 compared to CDEDNet-0.

5.2. Detection Results

The objective of using CDEDNet and HFRs data was to provide a summary of the eddy situation analysis and valuable suggestions to the local fisheries and seafaring in the Nanshan and Xuwen regions. After a comprehensive analysis of the detection results, the findings were summarized in the following three aspects.

The first was an overview of the eddy situation. During the 88 days, HFRs generated 5904 current maps, wherein 2123 current fields contained eddies. The current field maps with eddies were divided into three types: 1960 maps with a single-eddy, 147 with two eddies, and 16 with three eddies. The total number of eddies was 2301. Figure 8 depicts the current field with two or three eddies. After the eddy positions were determined from the masks, the streamlines in each mask region were calculated to indicate the internal eddy structure.

The second aspect was the relationship between the eddy radius and eddy number. Figure 9 illustrates the number of eddies with different radius. It could be concluded that the number of eddies decreased with the increment of radius. The radius of most eddies ranged from 4 km to 16 km and a small number of eddies had a radius larger than 30 km. As we know, smaller eddies appear more frequently since they can be easily generated by local disturbances. Thus, if a radar with a better sampling resolution is available, more eddies with a smaller radius may be observed. Because the observed region was in the off-shore area, two currents with opposite directions encountered in the area could intrude and wrap around each other, and gradually generate a small-scale eddy. With more opposite-direction currents joining, the scale of the eddy could gradually enlarge. However, considering that the topography of the sea-floor was not complicated and the off-shore area had a relatively stable environment, the number of current pairs with opposite directions was limited and only enough for generating eddies with a radius less than 32 km. Meanwhile, the number of cyclonic eddies was about 60 more than that of

anticyclonic eddies on each level of radius. However, there was no obvious relationship between the eddy type and eddy radius.

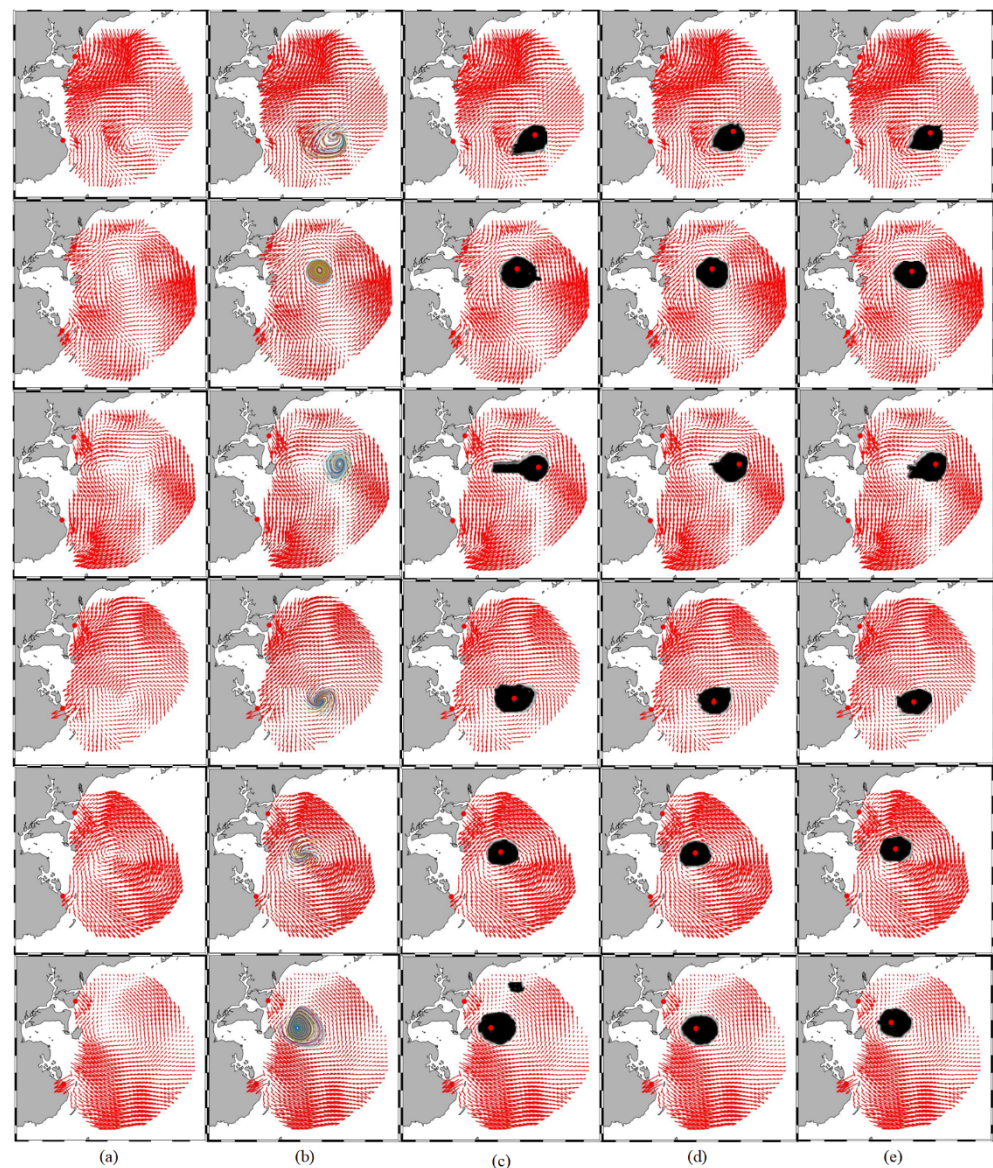


Figure 7. Comparison of eddy detection results. (a) Original current field; (b) Ground truth eddies; (c) Eddies detected by CEDENet-0; (d) Eddies detected by CEDENet-1; (e) Eddies detected by CEDENet-2. The rows are for different data times. From top to bottom: 11:20 28 July, 17:00 14 August, 8:40 25 August, 10:20 8 September, 21:40 27 September, and 12:20 12 October 2017. The dark regions indicate the boundaries of the detected eddies and the red spots depict the eddy centers.

Table 1. The accuracy and Intersection over Union (IoU) obtained by CEDENet-0, CEDENet-1, and CEDENet-2 on 30-times experiments.

Algorithm	Accuracy			Average Accuracy	Prediction Accuracy	IoU
	Cyclonic	Anticyclonic	None			
CEDENet-0	0.831	0.818	0.822	0.823	0.792	0.709
CEDENet-1	0.905	0.883	0.895	0.894	0.882	0.807
CEDENet-2	0.884	0.876	0.897	0.885	0.863	0.796

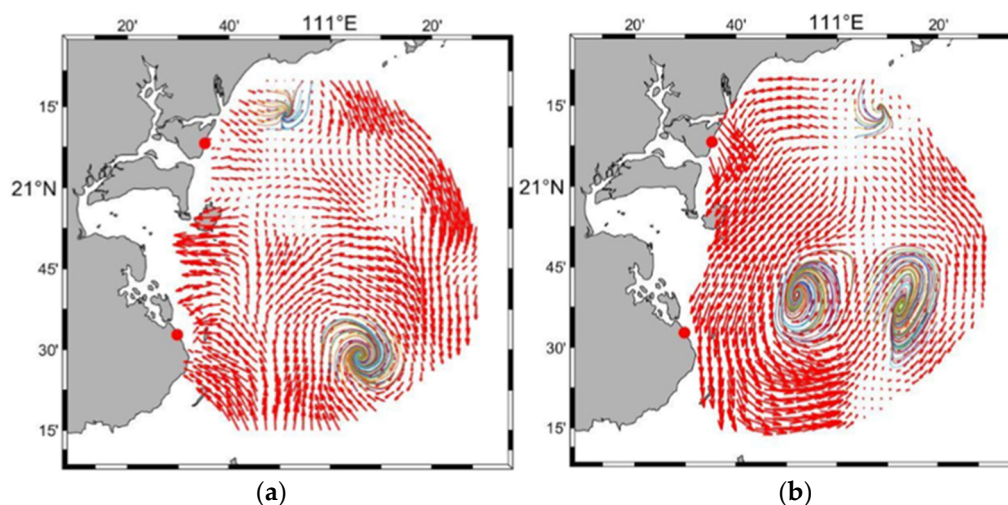


Figure 8. Special eddy situations. (a) Two eddies and (b) three eddies.

The third aspect was the occurring period of the eddy. It was found that 2301 eddies were evenly distributed at each period of 24 hours. Wherein, the two periods of 21:00 to 3:00 and 10:00 to 14:00 had a relatively higher possibility for the occurrence of smaller eddies. Considering that the eddy frequently occurred due to the fast change in temperature during these two periods, it suggested that the local marine activities should be reduced due to a possibly dangerous eddy.

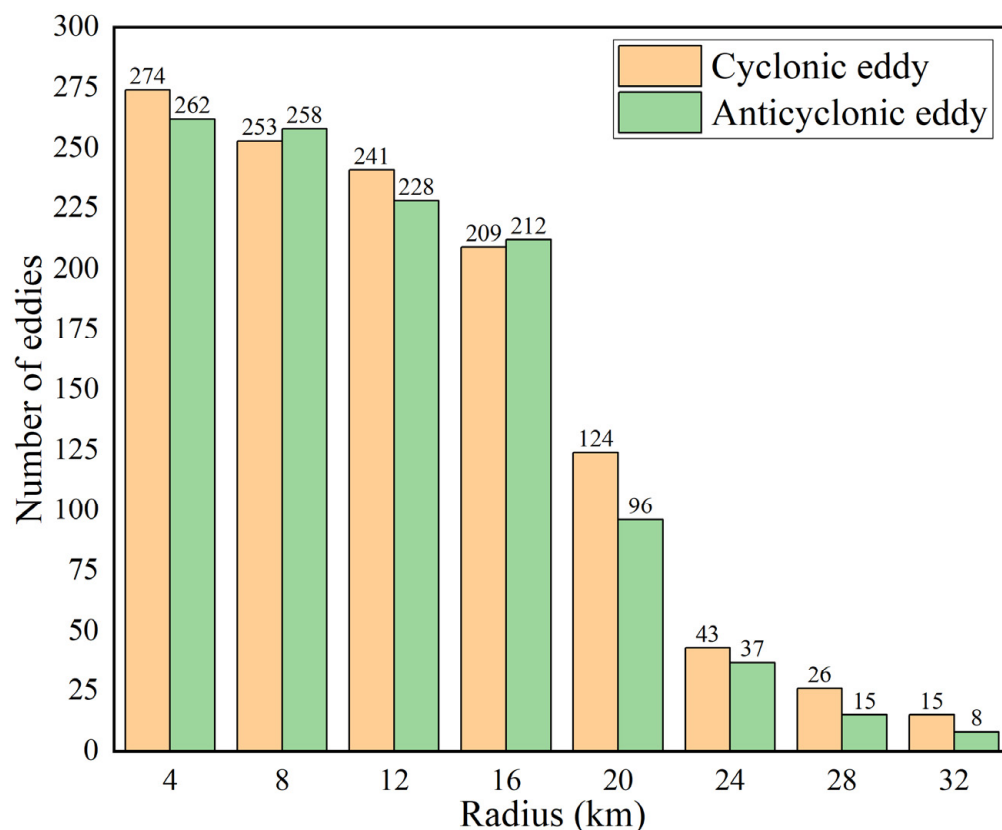


Figure 9. The relationship between eddy radius and eddy number.

5.3. Eddy Phenomenon

During the 88-days observation, the merging phenomenon of two eddies was also captured by the OSMAR-S radar. Although the mergers were extracted from different

periods, the different stages of the entire eddy merging process were recorded. Figure 10 shows four different merging stages of two eddies rotating in the same direction: encounter, contact, partial merger, and complete merger. In the encounter stage, the two eddies attracted each other and the distance between their centers decreased with time. In the contact stage, the outermost currents between two eddies interacted with each other, and then gradually merge into one current. In the partial merger stage, while the centers of two eddies approached each other, more and more inner currents of the eddy start to flow together into one layer. In the complete merger stage, the strong eddy wrapped around the weak one till the two eddies merged into one eddy. It is worth noting that two eddies rotating in opposite directions hardly merge (see Figure 11).

The radar also successfully observed the dynamic trajectory of the eddy with an automatic eddy tracking algorithm (when counting the number of eddies, the eddies belonging to the same trajectory were counted only once). Figure 12 depicts the eddy dynamic trajectory from 11:20 to 14:20 on 30 August 2017. The eddy was originated from the southeast part of the observed region. Then it gradually moved to near the center, which took about 1 h 20 min. After arriving near the central region, the eddy moved west toward the shore. Finally, it stayed at a distance from the shore and gradually became weaker with time.

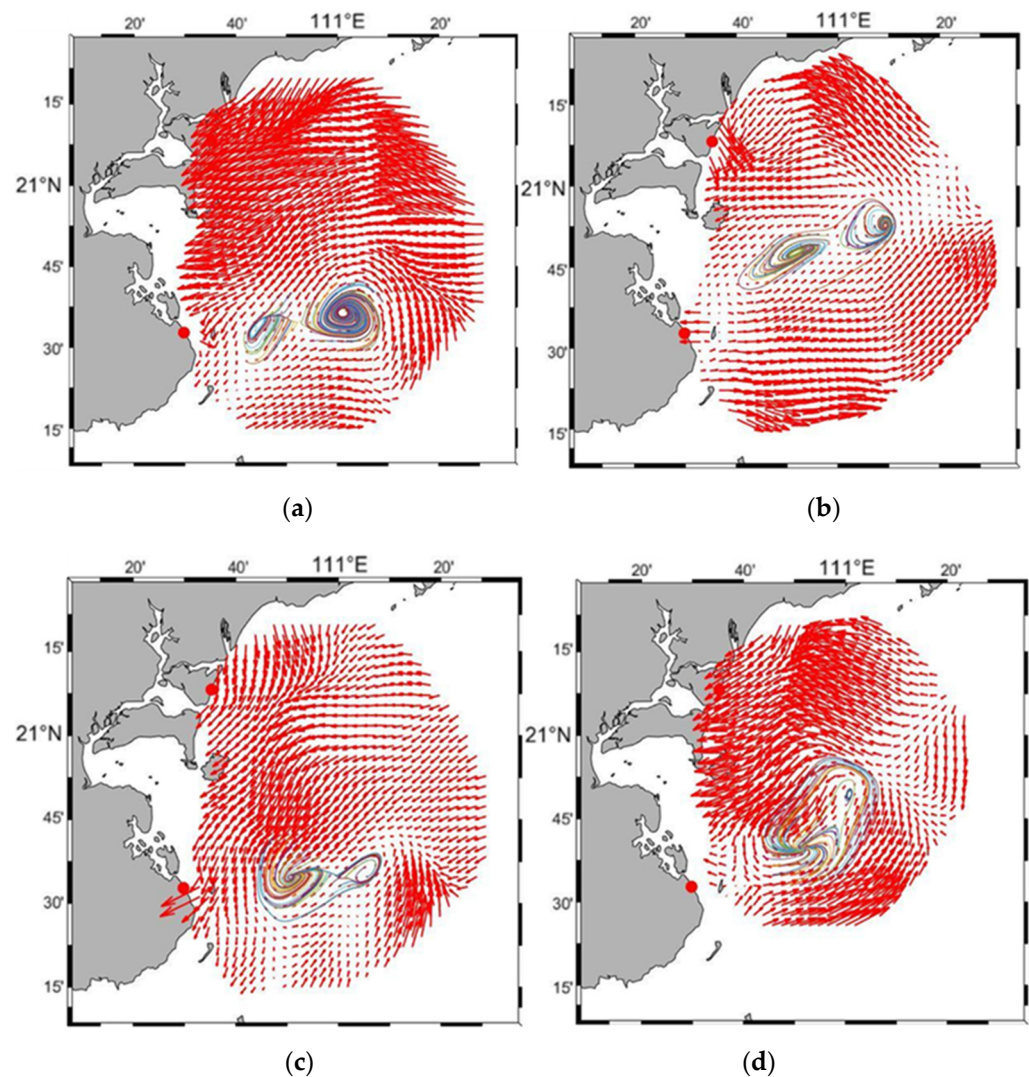


Figure 10. The four merging stages of two eddies rotating in the same direction. (a) Encounter (11:40), (b) contact (15:20), (c) partial merger (19:00), and (d) complete merger (22:40) on 1 October 2017.

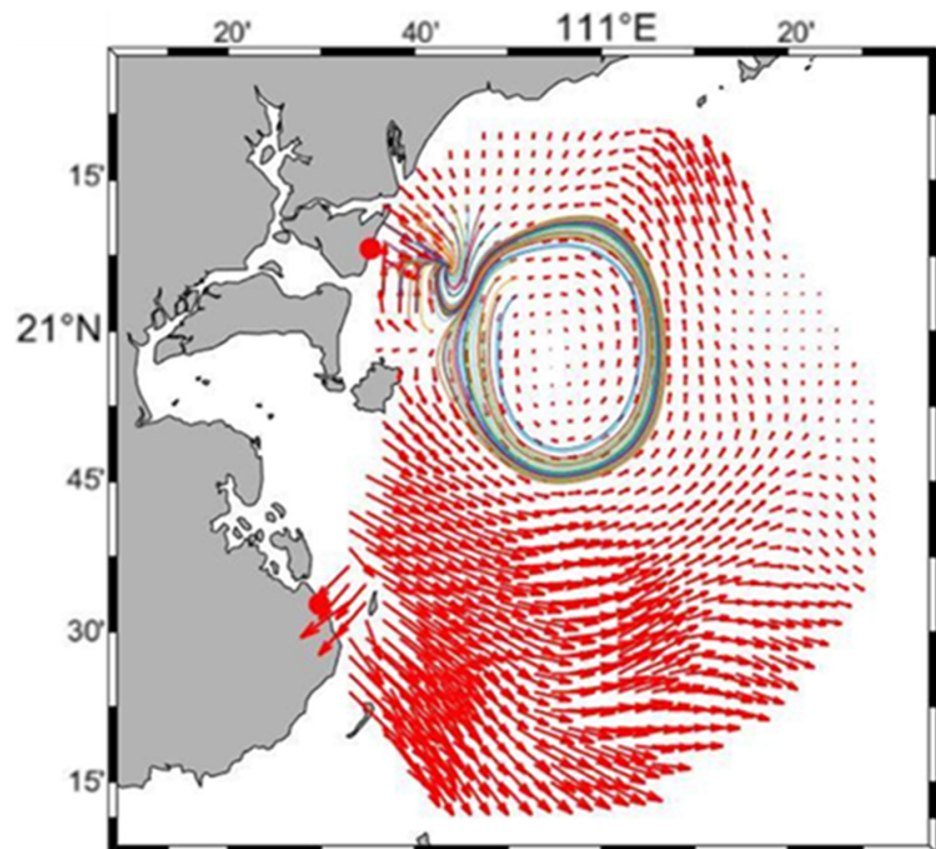


Figure 11. The case of two eddies rotating in opposite directions.

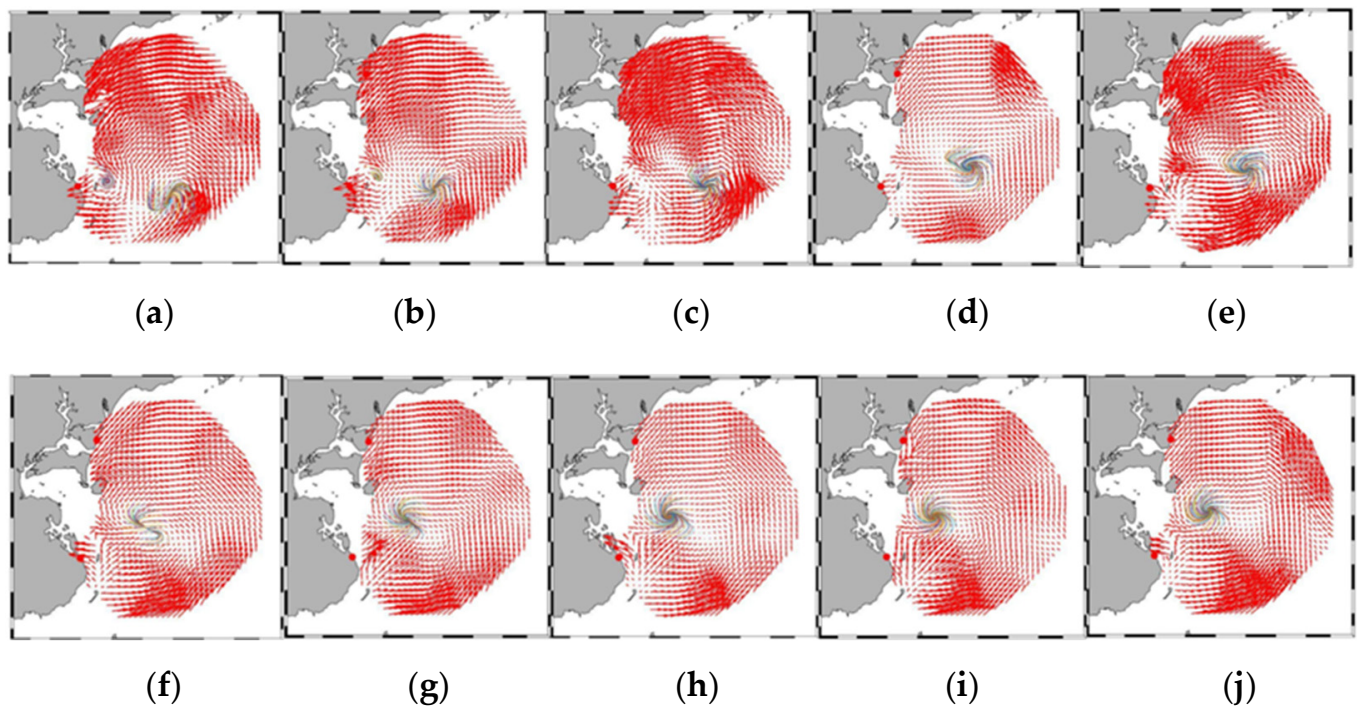


Figure 12. The eddy movement from 11:20 to 14:20, August 30, 2017. (a) 11:20, (b) 11:40, (c) 12:00, (d) 12:20, (e) 12:40, (f) 13:00, (g) 13:20, (h) 13:40, (i) 14:00, and (j) 14:20.

6. Conclusions

In this paper, in order to explore the eddy situation in Nansan and Xuwen, a cross-domain eddy detection neural network is constructed based on HFR field data. Three architectures are presented for handling different challenges in deep eddy detection. The first architecture, CDEDNet-0 uses an FCN-based network to extract deep-level eddy features and determine the eddy's location. The second architecture CDEDNet-1 incorporates an instance-based domain adaptation method to enlarge the training dataset to solve the problem of insufficient effective labeled data. The third architecture, CDEDNet-2 adopts parameter-based transfer learning for multi-scene eddy detection, which enables inheriting previous detection experience. The experiment demonstrates that CDEDNet-1 and CDEDNet-2 perform better than CDEDNet-0 in terms of accuracy. CDEDNet-1 and CDEDNet-2 have similar results in the segmentation index. Meanwhile, the analysis illustrates that an increased eddy radius leads to a decreased eddy number, and the eddy frequently occurs during two periods, 21:00 to 3:00 and 10:00 to 14:00, in the Nansan and Xuwen regions. The phenomena of eddy merger and eddy dynamic trajectory are also recorded and analyzed. The multi-eddy phenomenon is also recorded and discussed. The results of the eddy phenomenon investigation are significant for providing reasonable suggestions to local fishery and seafaring. Moreover, these results are expected to provide more observation data for physical oceanography researches on submesoscale eddies.

It should be pointed out that certain QC/QA measures have been taken while generating the datasets used in this study, but some outliers are still observed near the boundary and baseline of the radar sites. Although these outliers showed little impact on the eddy detection results in this study, more effort should be expended to develop more efficient QC/QA measures to enhance the reliability and accuracy of current measurement and eddy detection in the area near the boundary and baseline of the radar sites.

Our future work will consider but is not limited to the following directions. The first is to further test the effectiveness of the proposed method using more HFRs data collected from different regions and periods although the results based on the limited data used in this study show it performs well. The second is to investigate the transfer of multi-source heterogeneous models. The heterogeneous model can support different structures and parameters for network merging and improve model diversity. The third is to fuse data from other sensors (e.g., synthetic aperture radar) for eddies detection.

Author Contributions: Conceptualization, F.L. and H.Z.; methodology, F.L.; software, F.L.; data: B.W.; validation, W.H. and Y.T.; writing—original draft preparation, F.L.; writing—review and editing, H.Z. and W.H. All authors have read and agreed to the published version of the manuscript.

Funding: This research was funded by the National Natural Science Foundation of China, grant number 62071337, Key Program of Marine Economy Development (Six Marine Industries) Special Foundation of Department of Natural Resources of Guangdong Province (GDNRC [2020]010) and Guangdong Province Key Area Research and Development Program, grant 2020B1111020003. (Corresponding author: Hao Zhou.)

Data Availability Statement: The raw/processed data required to reproduce these findings cannot be shared at this time as the data also forms part of an ongoing study.

Acknowledgments: In this section, you can acknowledge any support given which is not covered by the author contribution or funding sections. This may include administrative and technical support, or donations in kind (e.g., materials used for experiments).

Conflicts of Interest: The authors declare no conflict of interest. The funders had no role in the design of the study; in the collection, analyses, or interpretation of data; in the writing of the manuscript, or in the decision to publish the results.

References

1. Nan, F.; Xue, H.; Xiu, P.; Chai, F.; Shi, M.; Guo, P. Oceanic eddy formation and propagation southwest of Taiwan. *J. Geophys. Res. Space Phys.* **2011**, *116*, 12045–12061. [[CrossRef](#)]
2. Rhines, P.B. Mesoscale Eddies. In *Encyclopedia of Ocean Sciences*; Steele, J.H., Ed.; Academic Press: Cambridge, MA, USA, 2001; pp. 755–767.
3. Chelton, D.B.; Schlax, M.G.; Samelson, R.M. Global observations of large oceanic eddies. *Geophys. Res. Lett.* **2007**, *34*. [[CrossRef](#)]
4. Ivanov, A.Y.; Ginzburg, A.I. Oceanic eddies in synthetic aperture radar images. *J. Earth Syst. Sci.* **2002**, *111*, 281. [[CrossRef](#)]
5. Kantha, L.H.; Tierney, C.C. Global baroclinic tide. *Prog. Oceanogr.* **1997**, *40*, 163–178. [[CrossRef](#)]
6. Kessler, R.C.; Douglas, S.G. A Numerical Study of Mesoscale Eddy Development over the Santa Barbara Channel. *J. Appl. Meteorol.* **2010**, *30*, 633–651. [[CrossRef](#)]
7. Xing, T.; Yang, Y. Three Mesoscale Eddy Detection and Tracking Methods: Assessment for the South China Sea. *J. Atmos. Ocean. Technol.* **2021**, *38*, 243–258. [[CrossRef](#)]
8. McWilliams, J.C. The nature and consequences of oceanic eddies. *Large Igneous Prov.* **2008**, *177*, 5–15.
9. Capet, X.; McWilliams, J.C.; Molemaker, M.J.; Shchepetkin, A.F. Mesoscale to submesoscale transition in the California Current System Part I: Flow structure, eddy flux, and observational tests. *J. Phys. Oceanogr.* **2008**, *38*, 29–43. [[CrossRef](#)]
10. Chelton, D.B.; Gaube, P.; Schlax, M.G.; Early, J.J.; Samelson, R.M. The Influence of Nonlinear Mesoscale Eddies on Near-Surface Oceanic Chlorophyll. *Science* **2011**, *334*, 328–332. [[CrossRef](#)]
11. McWilliams, J.C. Submesoscale currents in the ocean. *Proc. R. Soc. A Math. Phys. Eng. Sci.* **2016**, *472*, 20160117. [[CrossRef](#)] [[PubMed](#)]
12. Weller, D.I.; Law, C.S.; Marriner, A. Temporal variation of dissolved methane in a subtropical mesoscale eddy during a phytoplankton bloom in the southwest Pacific Ocean. *Prog. Oceanogr.* **2013**, *116*, 193–206. [[CrossRef](#)]
13. Lévy, M.; Ferrari, R.; Franks, P.J.S.; Martin, A.P.; Rivière, P. Bringing physics to life at the submesoscale. *Geophys. Res. Lett.* **2012**, *39*. [[CrossRef](#)]
14. Holland, W.R.; Lin, L.B. On the Generation of Mesoscale Eddies and their Contribution to the Oceanic General Circulation. I. A Preliminary Numerical Experiment. *J. Phys. Oceanogr.* **1975**, *5*, 642–657. [[CrossRef](#)]
15. Zu, Y.; Sun, S.; Zhao, W.; Li, P.; Liu, B.; Fang, Y.; Abu Samah, A. Seasonal characteristics and formation mechanism of the thermohaline structure of mesoscale eddy in the South China Sea. *Acta Oceanol. Sin.* **2019**, *38*, 29–38. [[CrossRef](#)]
16. Bagaglini, L.; Falco, P.; Zambianchi, E. Eddy Detection in HF Radar-Derived Surface Currents in the Gulf of Naples. *Remote Sens.* **2019**, *12*, 97. [[CrossRef](#)]
17. Goldfine, N.; Zilberstein, V.; Schlicker, D. Eddy-Current in situ Sensors for SHM. In *Encyclopedia of Structural Health Monitoring*; John Wiley and Sons Ltd: Hoboken, NJ, USA, 2009.
18. Oliveira, F.S.C.; Polito, P.S. Mesoscale eddy detection in satellite imagery of the oceans using the Radon transform. *Prog. Oceanogr.* **2018**, *167*, 150–163. [[CrossRef](#)]
19. Liu, F.; Zhou, H.; Huang, W.; Wen, B. Submesoscale Eddies Observation Using High-Frequency Radars: A Case Study in the Northern South China Sea. *IEEE J. Ocean. Eng.* **2021**, *46*, 624–633. [[CrossRef](#)]
20. Upadhyaya, B.R.; Yan, W.; Behraves, M.M. Development of a diagnostic expert system for eddy current data analysis using applied artificial intelligence methods. *Nucl. Eng. Des.* **1999**, *193*, 1–11. [[CrossRef](#)]
21. Zhang, L.; Deng, Q.; Machiraju, R.; Rangarajan, A.; Thompson, D.; Walters, D.K.; Shen, H.-W. Boosting Techniques for Physics-Based Vortex Detection. *Comput. Graph. Forum* **2014**, *33*, 282–293. [[CrossRef](#)]
22. Qin, D.; Wang, J.; Liu, Y.; Dong, C. Eddy analysis in the Eastern China Sea using altimetry data. *Front. Earth Sci.* **2015**, *9*, 709–721. [[CrossRef](#)]
23. Ye, Z.X.; Chen, Q.; Li, B.H.; Zou, J.F.; Zheng, Y. Flow structure segmentation for vortex identification using butterfly convolutional neural networks. *Int. J. Mod. Phys. B* **2020**, *34*, 2040121. [[CrossRef](#)]
24. Chang, Y.L.; Oey, L.Y. Analysis of STCC eddies using the Okubo–Weiss parameter on model and satellite data. *Ocean Dynam.* **2014**, *64*, 259–271. [[CrossRef](#)]
25. Nencioli, F.; Dong, C.; Dickey, T.; Washburn, L.; McWilliams, J.C. A Vector Geometry–Based Eddy Detection Algorithm and Its Application to a High-Resolution Numerical Model Product and High-Frequency Radar Surface Velocities in the Southern California Bight. *J. Atmos. Ocean. Technol.* **2010**, *27*, 564–579. [[CrossRef](#)]
26. Viikmäe, B.; Torsvik, T. Quantification and characterization of mesoscale eddies with different automatic identification algorithms. *J. Coastal Res.* **2013**, *165*, 2077–2082. [[CrossRef](#)]
27. Moschos, E.; Schwander, O.; Stegner, A. Deep-SST-Eddies: A Deep Learning Framework to Detect Oceanic Eddies in Sea Surface Temperature Images, In Proceedings of the IEEE International Conference on Acoustics, Speech and Signal Processing (ICASSP), Barcelona, Spain, 4–8 May 2020.
28. Franz, K.; Roscher, R.; Milioto, A.; Wenzel, S.; Kusche, J. Ocean Eddy Identification and Tracking Using Neural Networks. In Proceedings of the IGARSS 2018–2018 IEEE International Geoscience and Remote Sensing Symposium, Institute of Electrical and Electronics Engineers (IEEE), Valencia, Spain, 22–27 July 2018; pp. 6887–6890.
29. Du, Z.J.; Wang, W.K.; Wang, H.Z. Oceanic Mesoscale Eddy Detection Method Based on Deep Learning. *Remote Sens.* **2019**, *11*, 1921. [[CrossRef](#)]
30. Xu, G.J.; Cheng, C. Oceanic Eddy Identification Using an AI Scheme. *Remote Sens.* **2019**, *11*, 1349. [[CrossRef](#)]

31. Lguensat, R.; Sun, M.; Fablet, R.; Tandeo, P.; Mason, E.; Chen, G. EddyNet: A Deep Neural Network For Pixel-Wise Classification of Oceanic Eddies. In Proceedings of the IGARSS 2018–2018 IEEE International Geoscience and Remote Sensing Symposium, Institute of Electrical and Electronics Engineers (IEEE), Valencia, Spain, 22–27 July 2018; pp. 1764–1767.
32. Santana, O.J.; Hernandez-Sosa, D.; Martz, J. Neural Network Training for the Detection and Classification of Oceanic Mesoscale Eddies. *Remote Sens.* **2020**, *12*, 2625. [[CrossRef](#)]
33. Du, Y.; Song, W.; He, Q.; Huang, D.; Liotta, A.; Su, C. Deep learning with multi-scale feature fusion in remote sensing for automatic oceanic eddy detection. *Inf. Fusion* **2019**, *49*, 89–99. [[CrossRef](#)]
34. Lai, Y.; Zhou, H.; Zeng, Y.; Wen, B. Accuracy Assessment of Surface Current Velocities Observed by OSMAR-S High-Frequency Radar System. *IEEE J. Ocean. Eng.* **2017**, *43*, 1068–1074. [[CrossRef](#)]
35. Cai, J.; Zhou, H.; Huang, W.; Wen, B. Ship Detection and Direction Finding Based on Time-Frequency Analysis for Compact HF Radar. *IEEE Geosci. Remote Sens. Lett.* **2021**, *18*, 72–76. [[CrossRef](#)]
36. Tian, Y. Dual-Frequency Fully-Digital HF Ocean Radar: Development and Research on Related Issues. Ph.D. Thesis, Wuhan University, Wuhan, China, 2015.
37. Zhou, H.; Wen, B.; Wu, S. Dense radio frequency interference suppression in HF radars. *IEEE Signal. Process. Lett.* **2005**, *12*, 361–364. [[CrossRef](#)]
38. U.S. Integrated Ocean Observing System. *Manual for Real-Time Quality Control of High Frequency Radar Surface Currents Data: A Guide to Quality Control and Quality Assurance of High Frequency Radar Surface Currents Data Observations*; U.S. IOOS Project; U.S. Department of Commerce, National Oceanic and Atmospheric Administration, National Ocean Service, Integrated Ocean Observing System: Washington, DC, USA, 2016; p. 58. Available online: https://cdn.ioos.noaa.gov/media/2017/12/HFR_QARTOD_Manual_05_26_16.pdf (accessed on 20 June 2021).
39. Liu, F.; Zhou, H.; Wen, B. DEDNet: Offshore Eddy Detection and Location with HF Radar by Deep Learning. *Sensors* **2020**, *21*, 126. [[CrossRef](#)] [[PubMed](#)]